

ARTICLE OPEN



Electrochemically exfoliated phosphorene nanosheet thin films for wafer-scale near-infrared phototransistor array

Youngseo Jeon^{1,7}, Dongjoon Rhee^{1,7}, Bing Wu², Vlastimil Mazanek², In Soo Kim^{3,4}, Donghee Son^{3,5,6}, Zdeněk Sofer^{1,2} and Joohoon Kang^{1,3}✉

Two-dimensional (2D) black phosphorus (BP), or phosphorene, has recently emerged as a promising 2D semiconductor because of its *p*-type charge transport behavior and near-infrared photoresponsivity. However, the application of BP in practical electronic and optoelectronic devices is hindered by challenges in producing high-quality BP films over large areas. In this manuscript, we present a facile solution-based process to create wafer-scale BP films for fabrication of *p*-channel field-effect transistors that are responsive to near infrared light. Few-layer BP nanosheets are first exfoliated from the bulk crystal *via* electrochemical intercalation of cationic molecules and then vacuum-filtered through an anodic aluminum oxide membrane. The resulting BP film can be transferred onto an SiO₂-coated silicon substrate, thereby allowing for realization of field-effect transistors after electrode deposition and thermal annealing. The transistor array exhibits spatial uniformity in electrical performance with an average hole mobility of $\sim 0.002 \text{ cm}^2 \text{ V}^{-1} \text{ s}^{-1}$ and on/off ratio of 130. Furthermore, gate-induced modulation of the BP channel allows for enhancement in the photoresponsivity for 1550-nm light illumination up to 24 mA W^{-1} , which benefits the application of the phototransistor array for near infrared imaging.

npj 2D Materials and Applications (2022)6:82; <https://doi.org/10.1038/s41699-022-00360-2>

INTRODUCTION

Two-dimensional (2D) black phosphorus (BP), or phosphorene, has received significant attention as a promising 2D semiconducting material for applications in electronics and optoelectronics^{1–4}. Different from graphene, whose current cannot be effectively turned off because of its gapless electronic structure^{5,6}, BP possesses an electronic bandgap that allows for fabrication of field-effect transistors (FETs) with high on/off ratios^{1–3}, and also exhibits much higher charge carrier mobilities compared to transition metal dichalcogenides (TMDCs) commonly used as a semiconducting channel in 2D-material-based FETs^{7–9}. In addition, BP has a direct bandgap that can be widely tuned over the visible and near infrared (NIR) spectral ranges, from 0.3 eV in its bulk form to 2.0 eV for the monolayer¹⁰. The photoresponsivity for the NIR wavelengths, particularly 1550 nm, opens up opportunities for telecommunication and eye-safe light detection and ranging (LIDAR) technologies^{3,11}, which are difficult to be accessed by TMDCs because they exhibit bandgaps mostly in the visible regime. Besides the outstanding electrical and optoelectronic properties, the *p*-type semiconducting behavior is another important feature that motivates the use of BP for device applications. Since the majority of 2D semiconductors are *n*-type and BP exhibits a much higher hole mobility compared to other semiconducting 2D materials¹², BP can serve as a high-performance *p*-type semiconductor to realize complementary metal oxide semiconductor (CMOS) logic circuits and van der Waals heterostructures with unique device characteristics^{13,14}.

Similar to graphene and 2D TMDCs, electronic-grade BP has been most commonly produced by micromechanical exfoliation of bulk crystals using Scotch tape, which yields highly crystalline

few-layer BP microflakes that are several micrometers in lateral size^{1–4}. The micromechanically exfoliated BP demonstrated outstanding electrical performance with a field-effect hole mobility of $\sim 1000 \text{ cm}^2 \text{ V}^{-1} \text{ s}^{-1}$ and current on/off ratio of $\sim 10^5$ as well as high photoresponsivity to the NIR light (e.g. $\sim 1000 \text{ A W}^{-1}$ at 900 nm)^{1,15}. This method, however, is limited for realizing prototype devices for fundamental studies because of low exfoliation yield, lack of precision in controlling the layer number, and limited scalability^{1–4}. Alternatively, vapor-phase deposition techniques^{16–18} and liquid-phase exfoliation (LPE) processes¹⁹ have been widely investigated for the large-scale synthesis of 2D BP. Compared to the vapor-phase deposition that often involves rather complex and extreme growth conditions under vacuum^{16–18}, liquid-phase exfoliation (LPE) serves as a facile approach to mass produce BP nanosheets¹⁹. In particular, ultrasonication of BP crystals in organic solvents or deoxygenated water can break the van der Waals bonds and yield stable nanosheet dispersions that can be deposited on arbitrary substrates *via* solution processing^{19–22}. One drawback of the LPE process, however, is that the lateral size of the resulting nanosheets scales with their thickness²³. Therefore, BP nanosheets that are responsive to 1550 nm light (3–5 layers) are small ($< 200 \text{ nm}$)^{10,20,24}, which poses challenges in creating continuous films with thicknesses thin enough to be fully depleted or accumulated under gate bias²⁵. Furthermore, the charge transport within the film is substantially impeded because (1) inter-sheet junction resistances are significantly high since the nanosheets are mainly connected by edge-to-edge contacts and (2) the nanosheets are not closely aligned along the substrate²⁶.

¹School of Advanced Materials Science and Engineering, Sungkyunkwan University (SKKU), Suwon 16419, Republic of Korea. ²Department of Inorganic Chemistry, University of Chemistry and Technology Prague, Technická 5, 166 28, Prague 6, Czech Republic. ³KIST-SKKU Carbon-Neutral Research Center, SKKU, Suwon 16419, Republic of Korea. ⁴Nanophotonics Research Center, Korea Institute of Science and Technology (KIST), Seoul 02792, Republic of Korea. ⁵Department of Electrical and Computer Engineering, Center for Neuroscience Imaging Research, Institute for Basic Science (IBS), Suwon 16419, Republic of Korea. ⁶Department of Superintelligence Engineering, SKKU, Suwon 16419, Republic of Korea. ⁷These authors contributed equally: Youngseo Jeon, Dongjoon Rhee. ✉email: joohoon@skku.edu

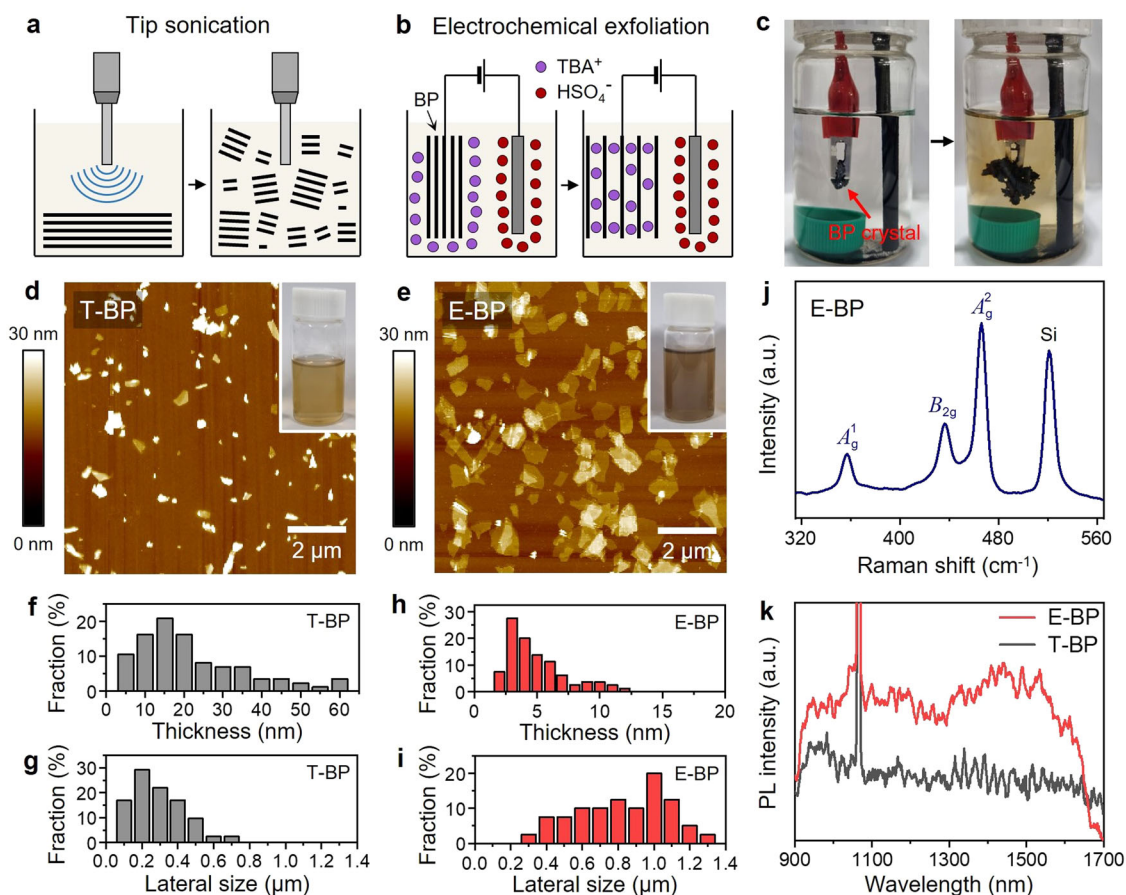


Fig. 1 Side-by-side comparison between tip-sonicated and electrochemically exfoliated BP nanosheets. **a, b** Schematic illustration of the two exfoliation methods. **c** Photographs of the BP crystal before and after electrochemically driven molecular intercalation. **d, e** AFM images of the tip-sonicated BP (T-BP) and electrochemically exfoliated BP (E-BP) nanosheets. Photographs of the dispersions are also provided as insets. **f** Nanosheet thickness and **g** lateral size histogram of T-BP. **h** Nanosheet thickness and **i** lateral size histogram of E-BP. **j** Raman spectrum of E-BP. **k** Photoluminescence spectra of T-BP and E-BP.

With the recent development of electrochemically driven exfoliation strategy^{27–29}, the production of 2D nanosheet dispersions with improved nanosheet morphology has been possible. This method has been established for various 2D materials such as graphene and TMDCs as well as BP^{30,31}. During the process, cationic molecules in the electrolyte intercalate into the BP crystal at the cathode and break van der Waals forces with minimal damage to the nanosheets, thereby producing few-layer BP nanosheets with much larger lateral sizes (hundreds of nanometers to over a micron) and a narrow thickness distribution. The resulting nanosheets exhibited a *p*-type behavior in FETs and achieved higher field-effect hole mobility and on/off ratio ($195 \text{ cm}^2 \text{ V}^{-1} \text{ s}^{-1}$ and 1.7×10^4)³⁰ compared to the liquid-phase-exfoliated counterparts ($25.9 \text{ cm}^2 \text{ V}^{-1} \text{ s}^{-1}$ and 1.6×10^3)²¹, and showed an excellent NIR photoresponsivity of 4.1 mA W^{-1} at 1550 nm ³¹. Although the electrochemical exfoliation strategy enhanced properties of the solution-based BP nanosheets, the application of the process for scalable device fabrication is still in its infancy because the previously reported FETs and photodetectors were demonstrated only at the single nanosheet level^{30,31}. Assembling the nanosheets into a continuous thin film will allow for the fabrication of devices over large areas, but achieving high electrical conductivity and photoresponsivity along with the gate tunability remains challenging because creating uniform, nanometer-scale thin films with small inter-sheet junction resistances is not trivial²⁶.

Here, we report a facile route to produce wafer-scale *p*-type 2D semiconductor films with NIR photoresponsivity based on the

solution-processed network of BP nanosheets. Dispersions of BP nanosheets that were predominantly 3–5 layers were first formed by electrochemical exfoliation of the bulk crystal using molecular intercalants. Vacuum-assisted filtration of the nanosheet dispersion through an anodic aluminum oxide (AAO) membrane created a uniform thin film of BP, which was transferred onto an SiO_2 -coated silicon substrate and deposited with electrodes to realize an array of FETs. By introducing a thermal annealing process, we could improve the contact between the electrode and BP and between BP nanosheets within the film *via* removal of phosphorus oxide and residual solvents, which enhanced the conductivity as well as gate tunability to achieve an average hole mobility of $\sim 0.002 \text{ cm}^2 \text{ V}^{-1} \text{ s}^{-1}$ and on/off ratio of 130. The gate-induced modulation of the BP channel from the fully off to fully on state allowed for the photoresponsivity to be enhanced by more than an order of magnitude, with the highest value of 24 mA W^{-1} for 1550-nm light illumination. Taking the advantage of the spatial uniformity in optoelectronic characteristics, the BP phototransistor array could be used for near-infrared imaging.

RESULTS

Structural and spectral characteristics of BP nanosheets

Figure 1a, b compares the conventional liquid-phase exfoliation (LPE) and our electrochemical exfoliation strategies used to obtain BP nanosheets. The liquid-phase-exfoliated nanosheets were produced by applying tip sonication to the bulk BP crystal in

anhydrous *N,N*-dimethylformamide (DMF) (Fig. 1a). During the sonication process, collapse of cavitation bubbles generated shock waves and microjets, which broke the van der Waals forces to exfoliate the crystal into nanosheets and also caused considerable fragmentation of the nanosheets^{32,33}. We denoted these nanosheets as tip-sonicated BP nanosheets (T-BP) for conciseness. Different from the case of LPE, the electrochemical exfoliation strategy was based on electrochemical potential-driven intercalation of tetrabutylammonium ions (TBA^+) in between the BP layers (Fig. 1b). The molecular intercalants effectively increased the inter-layer spacing, which was evidenced by the expansion of the BP crystal after the electrochemical intercalation (Fig. 1c). Because the inter-layer van der Waals forces were weakened by the presence of intercalants²⁹, the crystal could be exfoliated into nanosheets (E-BP) only after a mild sonication in poly(vinylpyrrolidone) (PVP) solution in DMF without significant nanosheet fragmentation. After the exfoliation, the as-prepared T-BP and E-BP dispersions were sequentially centrifuged at different rotational speeds to enrich well-exfoliated nanosheets having desired thicknesses (“Methods” and Supplementary Fig. 1). The first dispersions were produced by collecting the supernatant after centrifugation at $4590 \times g$ (denoted as $4590 \times g$ dispersion). The second batches were then prepared by re-dispersing the sediments in DMF, centrifuging the dispersion at $2340 \times g$, and acquiring the supernatant (denoted as $2340 \times g$ dispersion). Lastly, precipitates from the second centrifugation process were re-dispersed in DMF and then centrifuged at $840 \times g$. The resulting supernatant was used as the third dispersions (denoted as $840 \times g$ dispersion). After the centrifugation, nanosheets were rinsed with isopropyl alcohol (IPA) to remove PVP and DMF residues and finally re-dispersed in IPA. To minimize oxidation of BP, all the processes were performed using anhydrous solvents and in a nitrogen atmosphere.

To confirm the merit of the electrochemical exfoliation process to obtain 3–5 layered BP nanosheets that are responsive to 1550-nm light illumination, we compared the morphology of T-BP and E-BP nanosheets based on the atomic force microscopy (AFM). Figure 1d, e shows AFM images of the nanosheets that were cast on a SiO_2 -coated silicon substrate using the $2340 \times g$ dispersions. Compared to the case of T-BP (Fig. 1d), E-BP nanosheets showed much larger lateral sizes and smaller thicknesses (Fig. 1e). Based on the statistical analysis of the nanosheet dimensions, we confirmed that T-BP exhibited a broad distribution of thickness from a few nm to tens of nm (Fig. 1f), which suggests that the nanosheet assembly would show limited photoresponsivity under 1550-nm light excitation because of a broad distribution of bandgap. In addition, the lateral size of T-BP was only several hundreds of nanometers with an average value of 290 nm (Fig. 1g) and hence the nanosheets were not suitable for the formation of high-quality BP thin films. In contrast, E-BP showed a much narrower thickness distribution ranging from 2 to 12 nm (Fig. 1h). Significantly, the dispersion was predominantly composed of 3–6 nm-thick nanosheets, which corresponded to 3–5 layered BP considering that the reported thickness of the monolayer BP from the AFM measurement is ~ 1.5 nm³⁴. The lateral size of the E-BP was also much larger than that of T-BP with an average value of 830 nm (Fig. 1i). This large lateral size combined with the narrow thickness distribution highlights the advantage of using E-BP for producing large-area, high-quality semiconducting thin films for device applications.

E-BP nanosheets were further characterized with transmission electron microscopy (TEM) to confirm that the crystallinity of BP was maintained after the electrochemical exfoliation (Supplementary Fig. 2a). The high-resolution TEM image (Supplementary Fig. 2b) and selected area electron diffraction pattern (Supplementary Fig. 2c) clearly showed the crystal structure expected for BP nanosheets that were exfoliated along the [010] direction³⁵. The crystalline nature of E-BP was also corroborated by the Raman spectrum, in which three characteristic peaks corresponding to BP

phonon modes were present (Fig. 1j): A_1^1 , B_{2g}^2 , and A_2^2 peaks were located at 357 cm^{-1} , 436 cm^{-1} , and 466 cm^{-1} , respectively³⁶.

We then compared the photoluminescence (PL) spectra of T-BP and E-BP to investigate the effect of the exfoliation process on the luminescence properties of the resulting nanosheets. Figure 1k shows PL spectra of the nanosheet films on anodic aluminum oxide (AAO) membranes that were formed with $2340 \times g$ dispersions (“Methods”), where the sharp peak at 1064 nm corresponds to 1064-nm component from the 532 nm laser source³⁷. As expected from the AFM thickness measurement (Fig. 1h), E-BP exhibited a broad peak at ~ 1470 nm that spanned from 1300 to 1600 nm, which can be attributed to the light emission from 3–5 layered BP nanosheets^{10,24}. In contrast, T-BP did not show PL signal in the tested NIR region (up to 1700 nm) because the number of layers in the nanosheets was much larger and thus their bandgap was smaller than 0.73 eV (emission at wavelengths larger than 1700 nm). We also characterized the morphology and PL properties of BP nanosheets that were obtained from two other centrifugation processes ($840 \times g$ and $4590 \times g$). Interestingly, E-BP dominantly consisted of 3–6 nm-thick nanosheets for both $840 \times g$ and $4590 \times g$ cases and therefore exhibited a broad PL peak at ~ 1470 nm ranging from 1300 to 1600 nm similar to the case of $2340 \times g$ centrifugation (Supplementary Fig. 3). On the other hand, T-BP did not exhibit PL signals in the 1300–1600 nm spectral range. For the case of $840 \times g$ dispersion, the thickness of nanosheets ranged from tens of nm to hundreds of nm and thus PL emission was not observed for the tested NIR wavelengths. Although the film prepared with $4590 \times g$ dispersion showed a weak PL peak at ~ 900 nm that originated from BP nanosheets with thicknesses of several nm, there was no PL emission in the 1300–1600 nm spectral region.

Field-effect transistors from E-BP nanosheet films

The uniformity in thickness and large lateral size of E-BP nanosheets allowed for the formation of semiconducting thin films that are continuous over large areas (Fig. 2). In particular, E-BP nanosheets could self-assemble into a uniform BP thin film when the dispersion was vacuum-filtered through the AAO membrane (“Methods”). The resulting film could then be transferred onto a heavily doped silicon (p^{++}) substrate coated with a 300-nm SiO_2 dielectric layer for device fabrication. Figure 2a shows the BP film transferred on the SiO_2/Si substrate, which was formed with the supernatant from a single centrifugation step at $840 \times g$. Source and drain electrodes (channel length: 20 μm) were created by depositing gold (50 nm) through a shadow mask without defining the channel areas *via* photolithography to minimize the oxidation of BP. The resulting back-gate field-effect transistors were then annealed at 320 $^\circ\text{C}$ for 30 min to completely evaporate residual solvents and to improve the contact between the BP film and electrodes, after which the thickness of the BP film became ~ 20 nm (Fig. 2b). We confirmed that the film still exhibited characteristic Raman peaks and PL emission over 1300–1600 nm wavelengths, which indicates that the thermal annealing did not degrade BP (Fig. 2c, d).

The electrical properties of the BP film were drastically different before and after annealing. In particular, the as-prepared BP field-effect transistor was characterized by a super-linear current–voltage behavior under zero gate voltage (V_G), which can be attributed to the Schottky barrier formed at the electrode/BP contact^{1,38,39}. In addition, we observed that the device exhibited substantially low current levels: for example, the drain current (I_D) was only ~ 3 pA when the applied drain voltage (V_D) was 1 V (Fig. 2e). We believe that such a low current most likely resulted from the thin layers of phosphorus oxide formed on the surface of BP nanosheets (Supplementary Fig. 4a), which could function as tunneling barriers between the electrode and BP and between BP nanosheets within the

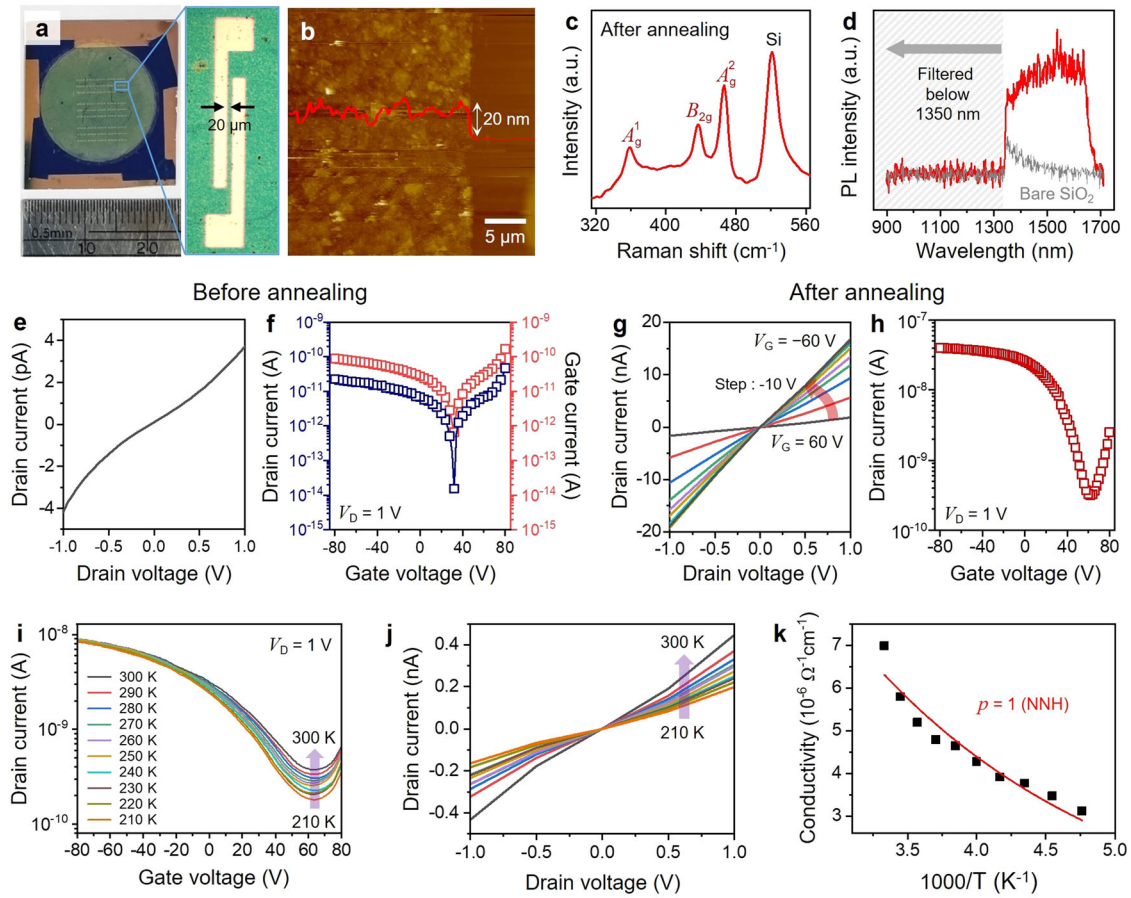


Fig. 2 Effect of annealing process on the electrical properties of the BP transistor. **a** Photograph of the BP transistor array. Zoomed-in optical microscope image shows a single device. AFM image at the boundary between the annealed BP thin film and bare substrate regions. The film thickness is about 20 nm. **c** Raman spectrum of the BP thin film after annealing. **d** Photoluminescence spectrum of the annealed BP thin film. Spectral region with wavelengths shorter than 1350 nm was filtered to remove signals from the SiO₂/Si substrate. **e, f** Output and transfer curves of the BP transistor before annealing. **g, h** Output and transfer curves of the BP transistor after annealing. **i, j** Transfer curves ($V_D = 1$ V) and output curves ($V_G = 0$ V) at different temperatures from 210 K to 300 K. **k** Temperature-dependent conductivities of the BP film determined from the ungated device ($V_D = 1$ V).

film^{40,41}. The device also showed a significant gate leakage current during the gate voltage (V_G) sweep from 80 V to -80 V ($V_D = 1$ V) and hence the measured drain current mostly resulted from the gate leakage (Fig. 2f). Even when a high drain bias was applied ($V_D = 10$ V), during which the drain current was sufficiently higher compared to the leakage current, the drain current was nearly constant over the tested gate voltage range because gate modulation of the BP channel was not possible (Supplementary Fig. 5). When the device was annealed at 320 °C, we noted that the phosphorus oxide was removed from the film (Supplementary Fig. 4b) because the temperature was above its sublimation temperature⁴². As a result, the device exhibited a linear current–voltage behavior for the small drain biases (V_D from -1 V to 1 V) (Fig. 2g), which indicates that the electrode and BP channel formed a low-resistance ohmic-like contact with a minor Schottky barrier^{1,39}. The current level was also significantly enhanced after annealing because the contact between BP nanosheets was improved after the removal of phosphorous oxide and residual solvents. Notably, we observed the expected p -type charge transport behavior in the transfer curve with the drain current effectively modulated by the gate bias (Fig. 2h) as well as a clear current saturation behavior in the output characteristics (Supplementary Fig. 6). The transistor array showed a spatial uniformity in device performance with the average hole mobility of ~ 0.002 cm² V⁻¹ s⁻¹ and current on/off ratio of ~ 130 (Supplementary

Fig. 7). We noted that the hole mobility was much lower compared to those of the previously reported BP transistors based on a single microflake ($60\text{--}1000$ cm² V⁻¹ s⁻¹)^{1–4,30,31,39,43–45}, which is most likely because (1) junction between the nanosheets can act as a barrier to the charge transport and (2) current paths within the BP nanosheet network would be much more complex compared to the case of single flake since preferred charge transport directions are different for each of the nanosheets because of their random orientations^{26,46,47}. However, our strategy offers a distinct advantage in high-throughput fabrication of BP transistor arrays since the BP film is continuous over wafer scale areas and hence multistep fabrication processes based on electron-beam lithography or photolithography are not needed.

To reveal the dominant charge transport mechanism within the BP channel, we analyzed the current–voltage characteristics measured at different temperatures. We focused our analysis only on the annealed device because the as-prepared counterpart exhibited significant gate leakage currents that resulted in unreliable data. Figure 2i, j shows the transfer and output curves of the annealed BP transistor under $V_D = 1$ V for a range of temperatures from 210 K to 300 K. As expected for a typical 2D semiconductor device^{48–52}, the current level increased when the temperature became higher. From the output characteristics of the device at $V_D = 1$ V, the electrical conductivities (σ) were

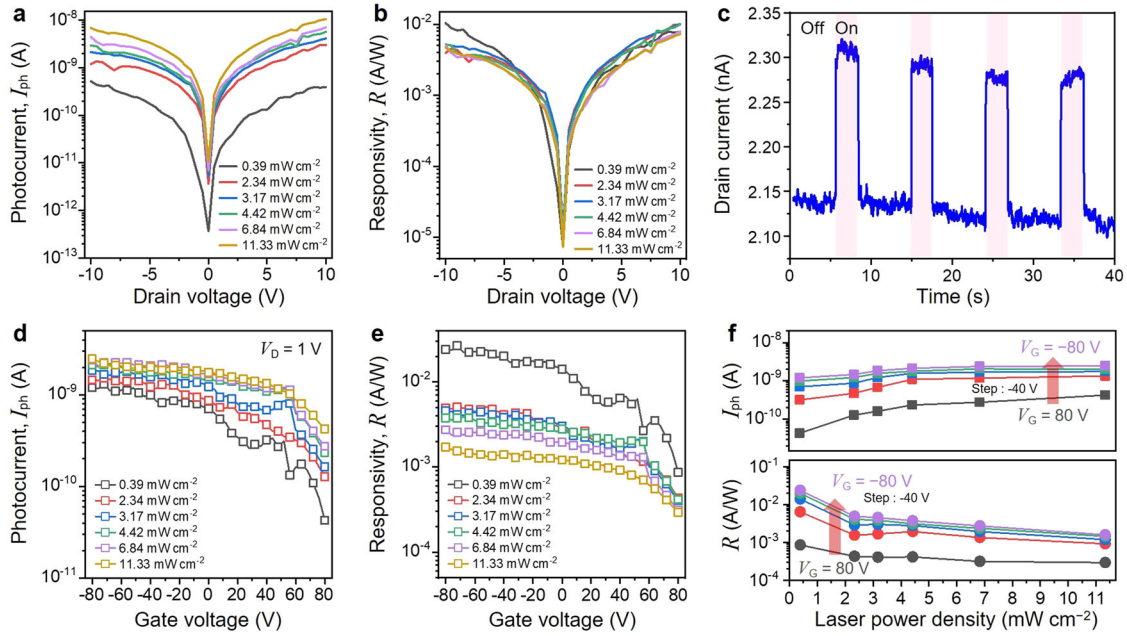


Fig. 3 Optoelectronic characteristics of the BP phototransistor under 1550 nm light source. **a** Photocurrent and **b** photoresponsivity under different power densities under zero gate bias condition. **c** Time-resolved photoresponse measured with $P = 2.34 \text{ mW cm}^{-2}$ and $V_D = 1 \text{ V}$. The 1550 nm light source was repeatedly turned on and off for 3 s and 7 s, respectively. **d** Photocurrent and **e** photoresponsivity under different power densities for different gate voltages ($V_D = 1 \text{ V}$). **f** Power-dependence of photocurrents and photoresponsivities for different gate voltages ($V_D = 1 \text{ V}$).

determined based on the following equation (Fig. 2k):

$$\sigma = \frac{L I_D}{Wt V_D} \quad (1)$$

where L is the channel length, W is the channel width, and t is the thickness of the BP channel⁵³. The electrical conductivity of the 2D semiconductor nanosheet network typically shows a characteristic temperature dependence:

$$\sigma(T) = \sigma_0 \exp \left[- \left(\frac{T_0}{T} \right)^p \right] \quad (2)$$

where T_0 is the characteristic temperature, σ_0 is the conductivity when the T approaches infinity, and p is an exponent that corresponds to a specific type of hopping mechanism^{53,54}. By plotting the conductivity as a function of inverse temperature and fitting the data to Eq. 2, we determined that the p value was 1. This result indicates that the dominant charge transport mechanism in our annealed BP film was nearest-neighbor hopping (NNH), during which charge carriers hop from flake to flake *via* spatially nearest available sites.

Optoelectronic response of E-BP transistors

Benefiting from the optical response of the BP film in the NIR spectral range, we could fabricate photodetectors that can detect 1550-nm light (Fig. 3). Figure 3a shows photocurrents measured by the BP photodetector under different optical power densities (P) without a gate bias, where the photocurrent (I_{ph}) was determined from the difference between the currents under dark (I_{dark}) and illumination (I_{light}) conditions ($I_{ph} = I_{light} - I_{dark}$). As expected, the photocurrent level became higher as the optical power density increased: for example, I_{ph} at $V_D = 10 \text{ V}$ increased from 0.4 to 10 nA when P increased from 0.39 to 11.33 mW cm^{-2} . We further investigated the characteristics of the BP phototransistor based on the photoresponsivity (R), which was determined by dividing the photocurrent by the optical power density times the effective illuminated area (S) ($R = I_{ph}/PS$). Overall, the device exhibited high NIR response with $R > 1 \text{ mA W}^{-1}$ for all tested

optical power densities when $V_D > 2 \text{ V}$ (Fig. 3b). Besides the steady-state optoelectronic properties, the temporal response of the device was also evaluated by measuring the drain current while the light illumination repeatedly turned on and off (Fig. 3c). The drain voltage and optical power density were fixed at $V_D = 1 \text{ V}$ and $P = 2.34 \text{ mW cm}^{-2}$, respectively. The device was characterized by an excellent response speed with the average rise and decay times of 5.1 ms and 6.8 ms, which were comparable to those of the previously reported BP photodetectors based on single microflakes^{15,55,56}. The gate-induced modulation of the electronic properties of our BP film allows for further tuning of the photoresponsivity (Fig. 3d, e). We noted that the BP phototransistor could generate positive photocurrents for all gate voltages we tested ($-80 \text{ V} \leq V_G \leq 80 \text{ V}$), with higher photocurrent levels for the on state of the BP channel (Fig. 3d). In particular, we achieved more than an order of magnitude tuning of the photoresponsivity from 0.86 mA W^{-1} to 24 mA W^{-1} by switching the transistor from the fully off ($V_G = 80 \text{ V}$) to fully on state ($V_G = -80 \text{ V}$) under 0.39 mW cm^{-2} illumination at $V_D = 1 \text{ V}$ (Fig. 3e). By plotting I_{ph} and R as a function of P (Fig. 3f), we found that the power exponent (α) for the photoresponsivity–power density relation ($R \propto P^{\alpha-1}$) was smaller than 1 at all gate voltages. This behavior indicates that photogating effect was present during the device operation⁵⁷, which is mostly likely because of trapping of electrons in the trap sites within the nanosheet network or at the BP/SiO₂ interface.

Gate-tunable E-BP photodetector arrays

The scalability of our electrochemical exfoliation and re-assembly strategy enables deterministic fabrication of BP phototransistor arrays for NIR light detection by simply depositing electrodes through a shadow mask without the alignment procedure (Fig. 4). Figure 4a, b shows the average I_{ph} and R of a 7×7 device array under 1550-nm light illumination at $P = 6.84 \text{ mW cm}^{-2}$ for different gate voltages ($V_D = 1 \text{ V}$). Because of the spatial uniformity of the BP film, the gate-voltage-dependence of I_{ph} and R was consistent across all the constituent devices.

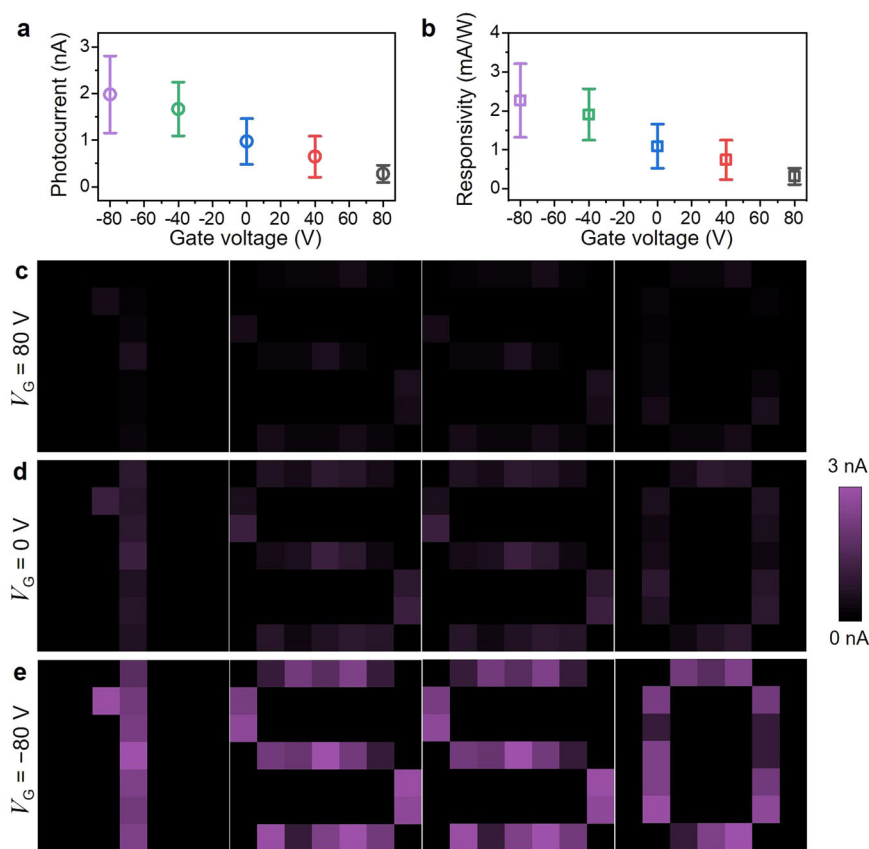


Fig. 4 Image sensing with the BP phototransistor array. **a** Average photocurrents and **b** photoresponsivities of the 7×7 array of phototransistors at different gate voltages. Error bars represent the standard deviation from 17–19 measurements. **c–e** Photocurrent mapping of a BP phototransistor array under 1550 nm light illumination ($P = 6.84 \text{ mW cm}^{-2}$) at $V_G = 80 \text{ V}$, 0 V , -80 V . The drain voltage was fixed at $V_D = 1 \text{ V}$.

Accordingly, the average I_{ph} and R values continuously changed from 0.28 nA and 0.31 mA W^{-1} at the fully-off state ($V_G = 80 \text{ V}$) to 1.98 nA and 2.3 mA W^{-1} at the fully-on state ($V_G = -80 \text{ V}$). To demonstrate the applicability of our BP phototransistor array for an image sensor, we also conducted spatial mapping of the photocurrent when the array was exposed to letter-shaped light illumination (“1”, “5”, “5”, and “0”). Figure 4c–e displays the photocurrent mapping under $V_G = 80 \text{ V}$, 0 V , and -80 V presented at the same photocurrent scale, where the letter patterns were clearly distinguished. As expected from the relation between the average photocurrent and gate voltage, the brightness of the images could be drastically modulated by gate voltage: the images were brightest for the $V_G = -80 \text{ V}$ case while they were darkest when $V_G = 80 \text{ V}$. This gate tunability in the imaging capability further highlights the benefit of the electrochemical exfoliation strategy in producing high-quality semiconducting BP thin films.

The performance and scalability of our BP devices compare favorably with those of other NIR detectors based on 2D materials synthesized by different methods (Supplementary Table 1)^{58–64}. Most of the previous reports are based on a single microflake, which only allows for the fabrication of a single or few devices and cannot be scaled up to realize large-scale photodetector arrays. Although our system achieved a lower photoresponsivity compared to many of the single 2D microflake-based devices, the performance is still significant considering that the carrier transport across the BP nanosheet network is more difficult compared to the case for a single flake because of the anisotropic electrical properties of constituent BP nanosheets. Moreover, our strategy is highly scalable and offers gate tunability to further engineer the photoresponsivity.

DISCUSSION

In summary, we demonstrated uniform gate-tunable BP films based on the electrochemical exfoliation of the bulk crystal and solution-based deposition process. Field-effect transistor arrays with p -type charge transport behavior and photoresponsivity to 1550-nm light could be realized over large areas, which was not possible with conventional liquid-phase exfoliated BP. The optoelectronic properties of the BP film could be effectively modulated by gate voltage, thereby offering flexibility in controlling the photoresponsivity of the array for near infrared imaging. Further enhancement in device performance will be possible by improving the lateral size of nanosheets and their stacking in the thin film network *via* optimization of the electrochemical exfoliation and solution-based deposition processes. We believe that our strategy will open a new route for fabricating devices for telecommunication and LIDAR applications as well as for realizing van der Waals heterostructures with unique electronic/optoelectronic characteristics.

METHODS

BP crystal growth

BP crystal was synthesized using a vapor-phase growth method reported in our previous work⁶⁵. Red phosphorus (2 g, 99.999%, Sigma-Aldrich, Czech Republic) was mixed with 120 mg of Sn and 60 mg of SnI_4 in a quartz glass ampoule (25 mm in inner diameter, 120 mm in length) and melt-sealed under high vacuum (1×10^{-3} Pa). The ampoule was placed horizontally in a muffle furnace and heated to 650°C over the course of 8 h, then cooled down to 400°C over 50 h and finally to room temperature over 25 h. The ampoule was opened in an Ar-filled glovebox, and the product

was washed with DMF and carbon disulfide several times and finally dried inside glovebox. SnI_4 was produced in chloroform by a direct reaction between Sn (99.999%, Sigma-Aldrich, Czech Republic) and iodine (99.999%, Sigma-Aldrich, Czech Republic), which was purified *via* recrystallization from chloroform.

Solution processing

For liquid-phase exfoliation using a tip sonicator, a BP crystal was loaded into a conical tube filled with anhydrous *N,N*-dimethylformamide (DMF). The sonicator tip was put inside the tube through a small hole perforated on the lid and then sealed with Parafilm in the glove box. The BP crystal was exfoliated by applying sonication at 40 W for an hour in an ice bath. For electrochemical exfoliation, we constructed a two-electrode cell by clipping the BP crystal at the cathode and placing the carbon electrode at the anode. Tetrabutylammonium bisulfate (Sigma-Aldrich) solution in anhydrous acetonitrile (concentration: 0.1 M) was used as an electrolyte. We applied a direct current under 8 V for 1 h to promote intercalation of molecules in between BP layers, while the whole cell was placed in a glove box to proceed the reaction in a nitrogen atmosphere. After the intercalation, the expanded BP crystal was bath sonicated in a poly(vinylpyrrolidone) (PVP) in anhydrous DMF (concentration: 22 mg/mL) for 30 min to exfoliate the BP nanosheets.

For nanosheet sorting, the as-exfoliated T-BP and E-BP dispersions were first centrifuged at $4590 \times g$ and then the supernatant was used as the first dispersions. After re-dispersing the precipitates in DMF, we proceeded with another centrifugation at $2340 \times g$ and collected the supernatant to produce the second dispersions. Similarly, the sediments from the second centrifugation process were redispersed in DMF and then centrifuged at $840 \times g$, after which the supernatant was obtained for creating the third dispersions. After sorting, PVP and DMF residues were rinsed by centrifuging the dispersions at $13480 \times g$ and re-dispersing the nanosheets in anhydrous isopropyl alcohol (IPA) for three times.

BP thin-film formation and phototransistor array fabrication

For thin film formation, BP nanosheets from a single centrifugation step at $840 \times g$ were collected by vacuum-assisted filtration on the anodized aluminum oxide (AAO) membrane with 25 nm pore size (Whatman Anodisc). The resulting BP thin film was transferred onto a heavily doped (p^{++}) silicon substrate coated with a 300-nm SiO_2 layer after etching the AAO membrane with phosphoric acid (20 wt%) for 6 h in N_2 atmosphere. Then, residual water was removed from the BP film by drying the sample in the vacuum chamber. To fabricate phototransistor array, we deposited 50 nm of gold using a thermal evaporator through a shadow mask with a channel length of 20 μm .

Materials characterization

The morphology of BP nanosheets was characterized using an atomic force microscope (Park Systems NX10). Raman and photoluminescence spectra were obtained by using a Alpha300R spectrometer (WITec) equipped with a 532-nm laser source. The power of 2 mW cm^{-2} was used. The chemical compositions of the samples were determined by X-ray photoelectron spectroscopy (XPS) using a monochromatic Al X-ray radiation source ($K_{\alpha 1} = 1486.7 \text{ eV}$) (Omicron Nanotechnology Ltd, Germany).

Device characterization

The electrical properties were measured using Keithley SCS-4200 system under vacuum ($\sim 7 \times 10^{-5}$ Torr) at room temperature. The temperature-dependent current–voltage characteristics were obtained using liquid nitrogen under vacuum. The photoresponses were measured using laser diodes (MLL-III-250L, 520L,

785L, 1060L, 1550L, BM LASER) as monochromatic light sources. For structured light illumination, letter-patterned shadow masks were used. Photocurrents measured on each device in the array were used to construct pixels.

DATA AVAILABILITY

The data that support the findings of this study are available from the corresponding author upon reasonable request.

Received: 8 July 2022; Accepted: 3 November 2022;

Published online: 15 November 2022

REFERENCES

- Li, L. et al. Black phosphorus field-effect transistors. *Nat. Nanotechnol.* **9**, 372–377 (2014).
- Liu, H. et al. Phosphorene: an unexplored 2D semiconductor with a high hole mobility. *ACS Nano* **8**, 4033–4041 (2014).
- Xia, F., Wang, H. & Jia, Y. Rediscovering black phosphorus as an anisotropic layered material for optoelectronics and electronics. *Nat. Commun.* **5**, 4458 (2014).
- Koenig, S. P., Doganov, R. A., Schmidt, H., Castro Neto, A. H. & Özyilmaz, B. Electric field effect in ultrathin black phosphorus. *Appl. Phys. Lett.* **104**, 103106 (2014).
- Schwierz, F. Graphene transistors. *Nat. Nanotechnol.* **5**, 487–496 (2010).
- Xia, F., Farmer, D. B., Lin, Y.-M. & Avouris, P. Graphene field-effect transistors with high on/off current ratio and large transport band gap at room temperature. *Nano Lett.* **10**, 715–718 (2010).
- Radisavljevic, B., Radenovic, A., Brivio, J., Giacometti, V. & Kis, A. Single-layer MoS_2 transistors. *Nat. Nanotechnol.* **6**, 147–150 (2011).
- Fivaz, R. & Mooser, E. Mobility of charge carriers in semiconducting layer structures. *Phys. Rev.* **163**, 743–755 (1967).
- Choi, W. et al. Recent development of two-dimensional transition metal dichalcogenides and their applications. *Mater. Today* **20**, 116–130 (2017).
- Castellanos-Gomez, A. Black phosphorus: narrow gap, wide applications. *J. Phys. Chem. Lett.* **6**, 4280–4291 (2015).
- Husko, C. et al. Silicon-phosphorene nanocavity-enhanced optical emission at telecommunications wavelengths. *Nano Lett.* **18**, 6515–6520 (2018).
- He, Q. et al. Quest for p-type two-dimensional semiconductors. *ACS Nano* **13**, 12294–12300 (2019).
- Tan, W. C. et al. Recent advances in black phosphorus-based electronic devices. *Adv. Electron. Mater.* **5**, 1800666 (2019).
- Shim, J. et al. Phosphorene/rhenium disulfide heterojunction-based negative differential resistance device for multi-valued logic. *Nat. Commun.* **7**, 13413 (2016).
- Huang, M. et al. Broadband black-phosphorus photodetectors with high responsivity. *Adv. Mater.* **28**, 3481–3485 (2016).
- Li, X. et al. Synthesis of thin-film black phosphorus on a flexible substrate. *2D Mater.* **2**, 031002 (2015).
- Smith, J. B., Hagaman, D. & Ji, H.-F. Growth of 2D black phosphorus film from chemical vapor deposition. *Nanotechnology* **27**, 215602 (2016).
- Wu, Z. et al. Large-scale growth of few-layer two-dimensional black phosphorus. *Nat. Mater.* **20**, 1203–1209 (2021).
- Woomer, A. H. et al. Phosphorene: synthesis, scale-up, and quantitative optical spectroscopy. *ACS Nano* **9**, 8869–8884 (2015).
- Yasaei, P. et al. High-quality black phosphorus atomic layers by liquid-phase exfoliation. *Adv. Mater.* **27**, 1887–1892 (2015).
- Kang, J. et al. Solvent exfoliation of electronic-grade, two-dimensional black phosphorus. *ACS Nano* **9**, 3596–3604 (2015).
- Kang, J. et al. Stable aqueous dispersions of optically and electronically active phosphorene. *PNAS* **113**, 11688–11693 (2016).
- Backes, C. et al. Equipartition of energy defines the size–thickness relationship in liquid-exfoliated nanosheets. *ACS Nano* **13**, 7050–7061 (2019).
- Yang, J. et al. Optical tuning of exciton and trion emissions in monolayer phosphorene. *Light Sci. Appl.* **4**, e312–e312 (2015).
- Kim, J. et al. Revisiting solution-based processing of van der Waals layered materials for electronics. *ACS Mater. Au* **2**, 382–393 (2022).
- Kelly, A. G., O'Suilleabhain, D., Gabbett, C. & Coleman, J. N. The electrical conductivity of solution-processed nanosheet networks. *Nat. Rev. Mater.* **7**, 217–234 (2022).
- Yang, S. et al. Ultrafast delamination of graphite into high-quality graphene using alternating currents. *Angew. Chem. Int. Ed.* **56**, 6669–6675 (2017).

28. Wang, C. et al. Monolayer atomic crystal molecular superlattices. *Nature* **555**, 231–236 (2018).
29. Lin, Z. et al. Solution-processable 2D semiconductors for high-performance large-area electronics. *Nature* **562**, 254–258 (2018).
30. Yang, S. et al. A delamination strategy for thinly layered defect-free high-mobility black phosphorus flakes. *Angew. Chem. Int. Ed.* **57**, 4677–4681 (2018).
31. Wang, N. et al. Electrochemical delamination of ultralarge few-layer black phosphorus with a hydrogen-free intercalation mechanism. *Adv. Mater.* **33**, 2005815 (2021).
32. Dhanabalan, S. C. et al. Emerging trends in phosphorene fabrication towards next generation devices. *Adv. Sci.* **4**, 1600305 (2017).
33. Telkhozhayeva, M. et al. Higher ultrasonic frequency liquid phase exfoliation leads to larger and monolayer to few-layer flakes of 2D layered materials. *Langmuir* **37**, 4504–4514 (2021).
34. Perello, D. J., Chae, S. H., Song, S. & Lee, Y. H. High-performance N-type black phosphorus transistors with type control via thickness and contact-metal engineering. *Nat. Commun.* **6**, 7809 (2015).
35. Zahn, D. et al. Anisotropic nonequilibrium lattice dynamics of black phosphorus. *Nano Lett.* **20**, 3728–3733 (2020).
36. Feng, Y. et al. Raman spectra of few-layer phosphorene studied from first-principles calculations. *J. Phys. Condens. Matter* **27**, 185302 (2015).
37. Nguyen, H. T. et al. Dislocations in laser-doped silicon detected by micro-photoluminescence spectroscopy. *Appl. Phys. Lett.* **107**, 022101 (2015).
38. Kamalakar, M. V., Madhushankar, B. N., Dankert, A. & Dash, S. P. Low Schottky barrier black phosphorus field-effect devices with ferromagnetic tunnel contacts. *Small* **11**, 2209–2216 (2015).
39. Du, Y., Liu, H., Deng, Y. & Ye, P. D. Device perspective for black phosphorus field-effect transistors: contact resistance, ambipolar behavior, and scaling. *ACS Nano* **8**, 10035–10042 (2014).
40. Edmonds, M. T. et al. Creating a stable oxide at the surface of black phosphorus. *ACS Appl. Mater. Interfaces* **7**, 14557–14562 (2015).
41. Shen, P.-C. et al. Ultralow contact resistance between semimetal and monolayer semiconductors. *Nature* **593**, 211–217 (2021).
42. Fan, S. et al. Rapid thermal thinning of black phosphorus. *J. Mater. Chem. C* **5**, 10638–10644 (2017).
43. Ling, Z.-P. et al. Black phosphorus transistors with near band edge contact Schottky barrier. *Sci. Rep.* **5**, 18000 (2015).
44. Tan, S. J. R. et al. Quasi-monolayer black phosphorus with high mobility and air stability. *Adv. Mater.* **30**, 1704619 (2018).
45. Li, J. et al. Ultrafast electrochemical expansion of black phosphorus toward high-yield synthesis of few-layer phosphorene. *Chem. Mater.* **30**, 2742–2749 (2018).
46. Lin, Z., Huang, Y. & Duan, X. Van der Waals thin-film electronics. *Nat. Electron.* **2**, 378–388 (2019).
47. Srivastava, P. K. et al. Resonant tunnelling diodes based on twisted black phosphorus homostructures. *Nat. Electron.* **4**, 269–276 (2021).
48. Siao, M. D. et al. Two-dimensional electronic transport and surface electron accumulation in MoS₂. *Nat. Commun.* **9**, 1442 (2018).
49. Kong, S., Wu, T., Zhuang, W., Jiang, P. & Bao, X. Realizing p-type MoS₂ with enhanced thermoelectric performance by embedding VMo₂S₄ nano-inclusions. *J. Phys. Chem. B* **122**, 713–720 (2018).
50. Ovchinnikov, D., Allain, A., Huang, Y.-S., Dumcenco, D. & Kis, A. Electrical transport properties of single-layer WS₂. *ACS Nano* **8**, 8174–8181 (2014).
51. Keyes, R. W. The electrical properties of black phosphorus. *Phys. Rev.* **92**, 580–584 (1953).
52. El-Mahalawy, S. H. & Evans, B. L. Temperature dependence of the electrical conductivity and hall coefficient in 2H-MoS₂, MoSe₂, WSe₂, and MoTe₂. *Phys. Status Solidi B* **79**, 713–722 (1977).
53. Piatti, E. et al. Charge transport mechanisms in inkjet-printed thin-film transistors based on two-dimensional materials. *Nat. Electron.* **4**, 893–905 (2021).
54. Xue, J., Huang, S., Wang, J.-Y. & Xu, H. Q. Mott variable-range hopping transport in a MoS₂ nanoflake. *RSC Adv.* **9**, 17885–17890 (2019).
55. Buscema, M. et al. Fast and broadband photoresponse of few-layer black phosphorus field-effect transistors. *Nano Lett.* **14**, 3347–3352 (2014).
56. Liu, Y., Cai, Y., Zhang, G., Zhang, Y.-W. & Ang, K.-W. Al-doped black phosphorus p–n homojunction diode for high performance photovoltaic. *Adv. Funct. Mater.* **27**, 1604638 (2017).
57. Fang, H. & Hu, W. Photogating in low dimensional photodetectors. *Adv. Sci.* **4**, 1700323 (2017).
58. Xie, Y. et al. Ultrabroadband MoS₂ photodetector with spectral response from 445 to 2717 nm. *Adv. Mater.* **29**, 1605972 (2017).
59. Gong, F. et al. Black phosphorus infrared photodetectors with fast response and high photoresponsivity. *Phys. Status Solidi RRL* **12**, 1800310 (2018).
60. Huang, H. et al. Highly sensitive visible to infrared MoTe₂ photodetectors enhanced by the photogating effect. *Nanotechnology* **27**, 445201 (2016).
61. Sharma, A., Srivastava, A. K., Senguttuvan, T. D. & Husale, S. Robust broad spectral photodetection (UV-NIR) and ultra high responsivity investigated in nanosheets and nanowires of Bi₂Te₃ under harsh nano-milling conditions. *Sci. Rep.* **7**, 17911 (2017).
62. Guo, J. et al. Few-layer geas field-effect transistors and infrared photodetectors. *Adv. Mater.* **30**, 1705934 (2018).
63. Shen, C. et al. Tellurene photodetector with high gain and wide bandwidth. *ACS Nano* **14**, 303–310 (2020).
64. Chai, R. et al. Non-layered ZnSb nanoplates for room temperature infrared polarized photodetectors. *J. Mater. Chem. C* **8**, 6388–6395 (2020).
65. Wang, L., Sofer, Z. & Pumera, M. Voltammetry of layered black phosphorus: electrochemistry of multilayer phosphorene. *ChemElectroChem* **2**, 324–327 (2015).

ACKNOWLEDGEMENTS

This study was supported by a National Research Foundation of Korea (NRF) grant funded by the Korean Government (MSIT) (2020R1C1C1009381). This project was also supported by the ERC-CZ program (project LL2101) from the Ministry of Education Youth and Sports (MEYS).

AUTHOR CONTRIBUTIONS

Y.J. and D.R. contributed equally to this work. Y.J., D.R., and J.K. conceived the idea and designed the experiments. Y.J. optimized the solution processing, fabricated devices, and performed characterizations. B.W., V.M., and Z.S. synthesized black phosphorus crystals. D.R., I.S.K., D.S., and J.K. analyzed spectra and current–voltage data. J.K. supervised the entire project. All authors wrote the manuscript and discussed the results at all stages.

COMPETING INTERESTS

The authors declare no competing interests.

ADDITIONAL INFORMATION

Supplementary information The online version contains supplementary material available at <https://doi.org/10.1038/s41699-022-00360-2>.

Correspondence and requests for materials should be addressed to Joohoon Kang.

Reprints and permission information is available at <http://www.nature.com/reprints>

Publisher's note Springer Nature remains neutral with regard to jurisdictional claims in published maps and institutional affiliations.



Open Access This article is licensed under a Creative Commons Attribution 4.0 International License, which permits use, sharing, adaptation, distribution and reproduction in any medium or format, as long as you give appropriate credit to the original author(s) and the source, provide a link to the Creative Commons license, and indicate if changes were made. The images or other third party material in this article are included in the article's Creative Commons license, unless indicated otherwise in a credit line to the material. If material is not included in the article's Creative Commons license and your intended use is not permitted by statutory regulation or exceeds the permitted use, you will need to obtain permission directly from the copyright holder. To view a copy of this license, visit <http://creativecommons.org/licenses/by/4.0/>.

© The Author(s) 2022